TAKYI-ANINAKWA, P., WANG, S., ZHANG, H., XIAO, Y. and FERNANDEZ, C. 2023. Enhanced multi-state estimation methods for lithium-ion batteries considering temperature uncertainties. *Journal of energy storage* [online], 66, article number 107495. Available from: https://doi.org/10.1016/j.est.2023.107495

Enhanced multi-state estimation methods for lithium-ion batteries considering temperature uncertainties.

TAKYI-ANINAKWA, P., WANG, S., ZHANG, H., XIAO, Y. and FERNANDEZ, C.

2023

OpenAIR @RGU

This document was downloaded from https://openair.rgu.ac.uk

CC BY NC ND

Enhanced multi-state estimation methods for lithium-ion batteries considering temperature uncertainties

Paul Takyi-Aninakwa [a,*], Shunli Wang [a], Hongying Zhang [a], Yang Xiao [a], Carlos Fernandez [b]

[a] School of Information Engineering, Southwest University of Science and Technology, Mianyang 621010, China
[b] School of Pharmacy and Life Sciences, Robert Gordon University, Aberdeen AB10-5GJ, United Kingdom

* Corresponding authors.
E-mail addresses: tapaul@mails.swust.edu.cn (P. Takyi-Aninakwa), 497420789@qq.com (S. Wang).

A B S T R A C T

Due to their high energy density and minimal emissions, lithium-ion batteries are frequently employed in electric vehicles (EVs). Accurate estimation of the micro-parameters, state of charge (SOC), and state of health (SOH) are a few primary monitoring functions of the battery management system (BMS) to increase the battery's efficiency and safety under various operating conditions. This paper proposes a SOC and SOH co-estimation method by adopting an ensemble empirical mode decomposition method with adaptive noise and an autoencoder (EEMDA) to extract, decompose, and reconstruct the full-scale charging voltage and current data for a dual extended Kalman filter (DEKF) with multi-parameter and time-scale updates for accurate estimation based on a variable forgetting factor limited memory recursive least squares (VFF-LMRLS) method. The VFF-LMRLS method is used to solve the data saturation phenomenon and identify the battery's characteristic micro-parameters based on a proposed dynamic migration second-order resistor-capacitor equivalent circuit model under different operating states. Battery tests are conducted at temperatures ranging from − 10 to 50 °C under complex working conditions. Using the VFF-LMRLS method, the effects of different temperatures on the micro-parameters are discussed. The SOC and SOH results of the proposed EEMDA-DEKF method based on the dynamic migration battery model show that the mean absolute error and root mean square error metrics have the least values of 0.0233% and 0.0252%, which signify an optimal performance improvement of 93.26% and 93.66%, respectively, compared to the conventional DEKF method. Based on the experimental results and analyses, the proposed method has a high degree of accuracy and robustness, which makes it feasible for battery monitoring and prognostic BMS applications.

Keywords:
State of charge; State of health; Dynamic migration second-order resistor- capacitor equivalent circuit model; Variable forgetting factor limited memory recursive least squares method; Ensemble empirical mode decomposition autoencoding method

1. Introduction

Because of the global energy crisis and the pressing need to reduce greenhouse gas emissions, clean energy has been promoted over the past few decades through the use of battery-powered devices [1]. One of the key functions of an energy storage system is to be a source of additional power when the main power source of the system cannot meet the power demands. Fuel cells [2], lithium-ion batteries [3], sodium-ion batteries [4], and other power battery types are currently among those with promising future development [5]. Nevertheless, lithium-ion batteries are used in a variety of applications, such as energy storage systems, electric transportation, portable electronic devices, electric vehicles (EVs), etc., because of **their unique properties, such as high power and energy density (up to 200 Wh/kg), high energy efficiency (more than 95%), relatively long cycle life (3000 cycles at a depth of discharge of 80%), no memory effects, a low self-discharge rate (5% per month), 95% recyclability after their end of life, etc. [6,7].**

Given the rapid advancement of EVs, it is crucial to have a reliable method for monitoring the battery's state of charge (SOC) and state of health (SOH), especially given that the energy and power of commonly used lithium-ion batteries decline with time [8,9]. Every lithium-ion battery experiences variations in resistance and capacity over its lifetime, which have an impact on the SOC and SOH during electro-chemical degradation processes that include active material decomposition, dendrite formation, the development of a solid electrolyte interface on the anode surface, etc. [10,11]. When the battery is fully charged or discharged, the SOC values are 100% or 0%, respectively. To ensure the reliability and safety of EVs and their users, it is essential to monitor the battery's SOH, which includes figuring out when the battery is getting close to the end of its useful life and how much power and energy it has left until that point [12,13]. Therefore, accurately estimating the SOC and SOH values provide information about the battery's charge and aging degree, which can be used to perform maintenance or reconfigure operational strategies to increase the service life. In addition, the battery management system (BMS) is developed to ensure effective monitoring of the external macro physical quantities (current, voltage, temperature, etc.) and states of lithium-ion batteries, including SOC and SOH estimation, to enhance the driving performance and safety of EVs, particularly safeguarding the battery from operational dangers, including overcharging and over-discharging [14–16].

Abbreviations: EV, Electric vehicle; SOC, State of charge; SOH, State of health; BMS, battery management system; 2RC-ECM, Second-order resistor-capacitor equivalent circuit model; OCV, Open-circuit voltage; DEKF, dual extended Kalman filter; EEMDA, Ensemble empirical mode decomposition autoencoding method; IMF, Intrinsic mode function; ME, Maximum error; MAE, Mean absolute error; RMSE, Root mean square error; VFF-LMRLS, Variable forgetting factor- limited memory recursive least squares; BBDST, Beijing bus dynamic stress test; DST, Dynamic stress test; HPPC, Hybrid pulse power characterization.

1.1. Review of battery state estimation methods

Several SOC estimation methods have recently been put forth by researchers, and they can be divided into four major categories: the Coulomb counting method, direct measurement methods, data-driven methods, and model-based methods [17,18]. To calculate the battery's remaining energy and determine its SOC, the Coulomb counting method uses the integral of the current flowing to and from the battery. Even though it is a simple open-loop method, its performance is sensitive to sampling noise and can hardly be used independently [19]. The direct measurement methods are based on parameter characterization to establish a stable relationship between the physical quantities of the battery and the measured state. They include open-circuit voltage (OCV), internal resistance, electrochemical impedance spectroscopy, etc. [20], and have been frequently employed for estimating the states of lithium-ion batteries. Even though these methods are simple and easy to implement [21], given the high dynamic operation load in mobile battery systems and the propensity for multi-use applications in stationary battery systems, the reliability of these direct measurement methods is reduced by the significant accumulated error caused by current sensor uncertainties, the infrequent correction periods, being highly sensitive to the battery's state and working conditions, etc. [22–25]. Data-driven methods based on active sensor data from the battery systems offer a potential direction [26]. These techniques use the battery as a "black box" with multiple layers and neurons to estimate SOC and SOH without creating a battery model. For instance, the gated recurrent unit [27,28], long short-term memory [29,30], convolutional neural network [23,31], extreme learning machine [32], support vector regression [33], etc., have been employed to estimate the SOC and SOH of lithium-ion batteries with satisfactory results. However, they mainly consider the electrophysical processes by approximating physical relations using a complex network structure, resulting in a high computation process [34], and those that have simple networking structures tend to have poor generalization ability [35]. Furthermore, they do not only need a large amount of data but are also very sensitive to the quality of the training data and process, resulting in the difficulty of selecting the characteristic hyper-parameters, which cannot guarantee accurate SOC and SOH estima-tion under complex and adverse working conditions [36].

The model-based methods, in contrast to the data-driven methods, take into account the physics of electrochemical processes using a battery model, such as the electrochemical model [37], the mechanistic model [38], the equivalent circuit model (ECM) [39], etc. The electrochemical model mainly includes a pseudo-two-dimensional (P2D) model, a single particle (SP) model, and a simplified pseudo-two-dimensional (SP2D) model. This model has good accuracy, but its complex partial differential equations have no analytical solutions, making it unsuitable for online applications [40]. The mechanistic model established for battery modeling obtains its parameters through excitation-response analysis based on internal physicochemical pro-cesses [38]. Generally, their computations are based on the finite difference method, which is time-consuming. The ECM uses electrical components, such as resistors, capacitors, and constant voltage sources, to form circuit networks to monitor and simulate the dynamic charac-teristics of the battery [41]. The ECM is currently in widespread use and has the benefits of having a clear physical meaning, simple mathemat-ical expression, less computational cost, etc. [42]. Model-based methods, such as the recursive Kalman filters [43–45], that are established based on ECMs have become a research hotspot for their simplicity, low computational complexity, real-time applicability, and robustness [46].

1.2. Literature review of existing methods

The SOC and SOH are the two macro-state quantities of the battery that are frequently focused on in nearly all applications, among others. The effectiveness of the battery system's control and mainte-nance operations is increased, and downtime is avoided through accurate SOC and SOH estimation. Additionally, it occasionally offers chances to increase a lithium-ion battery's useful life [47,48]. Even though considerable research has been conducted on estimating SOC and SOH individually, their estimations should be calculated collaboratively since they are substantially related to each other [49]. Liu et al. [50] proposed a co-estimation method for SOC and SOH using a particle filter based on the P2D model, which is mathematically complex with a time-delayed response for practical BMS applications. Qiao et al. [51] proposed a chaotic firefly-particle filtering method that realizes particle optimization by simulating the behavior of fire-flies in nature, which attract each other through light. It finds a new optimal solution by chaotically mapping a group of particles to different solution spaces to realize high-precision SOC and SOH co-estimations. However, this method is established based on a first-order migration ECM, whose performance under adverse conditions is not robust enough due to the inadequate micro-parameter characterization, and the adaptation of the proposed method to various temperatures is unverified [52]. Also, Wang et al. [53] proposed a backpropagation neural network-dual extended Kalman filter (DEKF) method based on the limited memory recursive least square (LMRLS) algorithm for SOC and SOH co-estimation of lithium-ion batteries. The backpropagation neural network is used to achieve synergistic estimation to improve the tracking accuracy of the DEKF method while taking into account the coupling effect between SOC and SOH. However, the verification of the proposed method is not conducted to test its robustness at various temperatures that significantly affect the performance of lithium-ion batteries. Li et al. [54] proposed an adaptive extended H-infinity filtering method with a particle swarm optimization network, which innovatively exploits the monitoring of the aging characteristics of the battery in terms of capacity and power fade for SOC and SOH estimation. Zou et al. [55] co-estimated the SOC and SOH using two EKFs with different time scales based on a first-order resistor-capacitor (1RC) ECM. The degradation performance of the nominal model over the battery's lifetime is quantified based on ECMs with fixed model parameters. As the battery's capacity reflects the SOH, Xiong et al. [56] co-estimated the SOC and capacity for lithium-ion batteries using a multi-stage model fusing method by considering the normal distribution, the mean, and variance of the residual error under a complex working condition. Also, Wei et al. [57] established a multi-timescale KF estimator for the co-estimation of the SOC and capacity based on an online identification method. However, the model parameters are affected by many factors, such as temperature, charge-discharge rates, SOC, working conditions, etc.[58], which are not considered. Since the aforementioned nonlinear factors have adverse effects on the battery and its estimated states in real-world applications, the estimation accuracy of these methods may significantly decline in the absence of model adaptation [59]. Additionally, these models tend to be accurate early in the battery's service life, but if the model parameters are fixed, they may not be able to adapt to changes in temperature and working conditions. In this regard, battery models with adaptive parameters are more futuristic for the multi-state estimation of lithium-ion batteries.

1.3. Contributions of this paper

First, this paper addresses the uncertainties from a different perspective by analyzing the sensitivity of each parameter and augmenting the dominant parameter as a new state to simultaneously estimate the SOC and SOH of lithium-ion batteries considering different temperatures based on the DEKF method. However, due to the nonlinear effects of temperatures on accurately co-estimating the SOC and SOH, this paper adopts an ensemble empirical mode decomposition (EEMD) method with adaptive noise to extract and decompose the original data, which is an improved variant of the empirical mode decomposition. Then, a multi-functional autoencoder is established to reconstruct the extracted features of the EEMD for the DEKF method, which is based on a proposed dynamic migration 2RC-ECM whose parameters are identified online using a variable forgetting factor (VFF)-LMRLS method for the multi-state estimation of lithium-ion batteries. The contributions of this paper are four-fold:

1 A dynamic migration battery model is proposed for online battery modeling to ensure the adaptation of the battery model to various working conditions. The long-term co-estimation accuracy of this model is enhanced by its construction on top of a predetermined 2RC-ECM.

2 The effects of data saturation caused by historical data are overcome by the VFF-LMRLS method to ensure accurate battery modeling and multi-state estimation for lithium-ion batteries. The characteristic micro-parameter estimation results accurately illustrate the dynamic changes of the battery at different temperatures.

3 Using the EEMD method, the current, voltage, and temperature inputs are effectively extracted and decomposed into signals with various features so that the autoencoder can reconstruct them for accurate SOC and SOH co-estimation at different temperatures and working conditions.

4 The proposed EEMDA-DEKF method provides more accurate results because it can compensate for noise measurements and models without requiring an initial SOC value and temperatures. Also, it has high superiority, accuracy, and robustness compared to the con-ventional DEKF method.

1.4. Outline of this paper

After the introduction and presentation of the state-of-the-art SOC and SOH estimation methods, the implementation of the battery model and the description of the mathematical methods are given in Section 2.

The battery and temperature tests are described in Section 3. Following this, the results of the battery model verification, the output of the micro-parameters, and the co-estimation results are presented and discussed. Finally, Section 5 is the conclusion of this paper and future work.

2. Optimized battery modeling and co-estimation methods

This section focuses on model verification and parameter un-certainties to maximize the agreement between model estimation and experimental data. To implement battery SOC and SOH co-estimation, first, an accurate battery model is constructed. Then, the optimized estimation method for accurate co-estimation is developed to ensure the safe and reliable operation of the lithium-ion battery.

The SOC indicates the ratio of the current capacity to the maximum possible charge that can be stored in the battery. Generally, SOC is ob-tained using the Coulomb counting method, which is expressed in Eq. (1).

$$SOC_k = SOC_0 - \frac{\int_0^k \eta I_{L,k} dk}{Q_n} \quad (1)$$

In Eq. (1), SOC_0 and SOC_k are the SOC values at time steps 0 and k, respectively. η is the Coulombic efficiency, which is defined as 1, I_L, k is the load current value at time step k, and Q_n is the battery's nominal capacity.

Without a SOH estimation or update by the BMS, the user will experience an overestimated range or less acceleration. The SOH manifests as capacity fading and internal resistance increasing, both of which change gradually in practical applications [55]. Typically, the changes in the battery's resistance, maximum power, or discharge capacity are used to define the SOH. Therefore, this paper considers the capacity-based definition, which is expressed in Eq. (2).

$$SOH = Q_k / Q_n * 100\% \quad (2)$$

In Eq. (2), Q_k is the remaining capacity at time step k, and Q_n is the nominal capacity of the battery. Usually, the charge and discharge methods are used to calculate both capacities. The nominal capacity is frequently substituted with the actual initial capacity, particularly when the analysis is not performed on the system as a whole [60].

2.1. Architecture of the lumped dynamic migration battery model

ECMs are composed of resistors and capacitors, which are widely used to monitor and simulate the internal characteristics of the battery in BMSs and other energy management systems due to their simple model structure and computation with good accuracy and reliability [61].

The conventional 2RC-ECM comprises three main components: (i) The voltage source is the first component. It uses U_{oc} to denote the ideal voltage source. (ii) The second component is the internal ohmic resistance, R_0. It represents the charge accumulation and dissipation in the electrical double layer as well as the electrical resistance coming from different battery components. (iii) The last two circuit components, respectively, conduct electrochemical-concentration polarization resistance and capacitance effects as well as the dynamic voltage responses.

Based on Kirchhoff's circuit law, the discrete-time state-space description of the electrical characteristics for the SOC and SOH co-estimation based on the 2RC-ECM is expressed in Eq. (3).

$$\begin{cases} U_{T,k+1} = U_{oc} - I_{L,k}R_0 - U_{p1,k} - U_{p2,k} + v_k \\ \begin{bmatrix} SOC_{k+1} \\ U_{p1,k+1} \\ U_{p2,k+1} \end{bmatrix} = \begin{bmatrix} 1 & 0 & 0 \\ 0 & exp\left(-\dfrac{\Delta k}{C_{p1}R_{p1}}\right) & 0 \\ 0 & 0 & exp\left(-\dfrac{\Delta k}{C_{p2}R_{p2}}\right) \end{bmatrix} \begin{bmatrix} SOC_k \\ U_{p1,k} \\ U_{p2,k} \end{bmatrix} + \begin{bmatrix} -\dfrac{\eta \Delta k}{3600Q_n} \\ R_{p1}\left(1 - exp\left(-\dfrac{\Delta k}{\tau_1}\right)\right) \\ R_{p2}\left(1 - exp\left(-\dfrac{\Delta k}{\tau_2}\right)\right) \end{bmatrix} I_{L,k} + w_k \\ Q_{k+1} = Q_k + R_k \end{cases} \tag{3}$$

In Eq. (3), Δk is the sampling time interval, and $[SOC_{k+1}, U_{p1,\ k+1}, U_{p2,\ k+1}]^T$ is defined as the state variable. U_{oc} is the OCV of the battery, which has a functional relationship with the SOC and U_L is the battery's terminal or closed-circuit voltage when connected to an external circuit. $I_{L,\ k}$ is the load current flowing through the 2RC-ECM (Assuming positive is discharging, and negative is charging). R_0 is the internal ohmic resistance, R_{p1} and R_{p2} are the electrochemical and concentration polarization resistances, respectively. C_{p1} and C_{p2} are the electrochemical and concentration polarization capacitances, respectively, of the bat-tery. $U_{p1,\ k}$ and $U_{p2,\ k}$ are the resultant voltage across the respective polarized resistor and capacitor circuit networks at time step k. Q_k is the actual capacity of the battery measured during the capacity calibration experiment at time step k. w_k and v_k are the process noise (R) and measurement noise (Q) assumed to be from zero-mean multivariate Gaussian white noise matrices.

A 2RC-ECM with dual RC circuits is constructed as the initial model, which is then used to establish the dynamic migration 2RC-ECM. This allows for the creation of a lithium-ion battery model that can accurately characterize the battery under various working states, as shown in Fig. 1.

To achieve the dynamic migration model of the initial battery model under various operation states, the OCV-SOC relationship curve of parameter dynamic change of the initial battery model can be reset online through linear transformations. The SOC obtained during the estimation process has a functional relationship with the reset initial model relationship curve. Therefore, to ensure that the dynamic migration model's parameters are relative to the actual battery model parameters, the inaccurate SOC must be corrected. In reality, batteries come in hundreds of different varieties, some of which are still under development. Therefore, a straightforward but effective linear migration is the best option. A superscript R is used to characterize the parameters of the migration battery model and base model. The state-space expression of the dynamic migration battery model, which is based on the 2RC-ECM, is shown in Eq. (4).

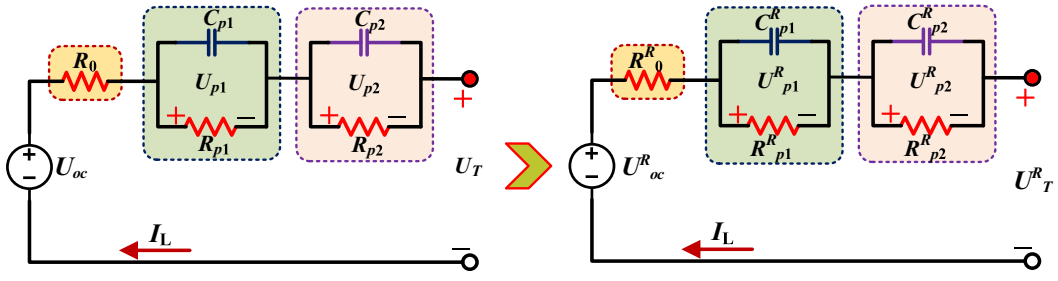

(a) Conventional 2RC-ECM (b) Dynamic migration 2RC-ECM

Fig. 1. The architecture of the dynamic migration battery model.

$$\begin{cases} Z = [z_1, z_2, z_3, \ldots, z_{10}\,] \\ SOC_k^R = z_1 SOC_k + z_2 \\ U_{oc,k}^R = g_{U_{oc}}(s) = z_3 f_{u_{oc}}\left(SOC_k^R\right) + z_9 \\ R_{0,k}^R = g_{R_0}(s) = z_4 f_{R_0}\left(SOC_k^R\right) + z_{10} \\ R_{p1,k}^R = g_{R_{p1}}(s) = z_5 f_{R_{p1}}\left(SOC_k^R\right) + z_{11} \\ R_{p2,k}^R = g_{R_{p2}}(s) = z_6 f_{R_{p2}}\left(SOC_k^R\right) + z_{12} \\ C_{p1,k}^R = g_{C_{p1}}(s) = z_7 f_{R_{p1}}\left(SOC_k^R\right) + z_{13} \\ C_{p2,k}^R = g_{C_{p2}}(s) = z_8 f_{R_{p2}}\left(SOC_k^R\right) + z_{14} \\ U_{T,k}^R = g_{U_{oc}}(I_{1:k}) = U_{oc,k}^R - I_{L,k} R_{0,k}^R - U_{p1,k}^R - U_{p2,k}^R + v_k \end{cases} \tag{4}$$

In Eq. (4), the migration model expression $Z = [z_1, z_2, z_3, \ldots, z_{14}]$ are the migration factors of the battery model to be determined, and SOC_k^R is the corrected SOC_k value. $R_{0,\,k}^R$, $R_{p1,\,k}^R$, $R_{p2,\,k}^R$, $C_{p1,\,k}^R$, and $C_{p2,\,k}^R$ are the micro-parameter values obtained after migration of the relationship curve of the battery's micro-parameters and SOC-SOH values. $U_{T,\,k}^R$ is the closed-circuit or terminal voltage value determined by the observation equation of the dynamic migration battery model.

2.2. Integrated VFF-LMRLS parameter identification method

To identify the micro-parameters of the dynamic migration battery model in a computationally efficient manner, the model parameters are estimated online and then mapped to the actual state of the battery. The parameter estimation method is a mathematical method to determine model parameters using collected battery data and a known model structure. The RLS algorithm is straightforward and useful, obtaining real-time characteristics by continuously updating and correcting the system parameters. However, as iteration times and data volumes rise, the "data saturation" phenomenon emerges. This occurs as a result of the increase in the amount of data, which affects the gain matrix using the old data and gradually tends to zero, causing the recursive ability to correct errors to slowly degrade [62]. As a result, this paper develops the VFF-LMRLS method based on the LMRLS method, in which the old data is removed when new data is input and only the most recent limited- length data is used for parameter estimation. The recurrence principle is mathematically expressed as follows:

Set the initial value and get the parameter estimation value for the memory interval using the iterative RLS algorithm shown in Eq. (5).

$$\begin{cases} \widehat{\theta}(k) = \widehat{\theta}(k-1) + K(k|k-1)\left[y(k|k-1) + \varnothing^T(k)\widehat{\theta}(k)\,\right] \\ K(k) = P(k)\varnothing(k)\left[\varnothing^T(k)P(k)\varnothing(k) + 1\,\right]^{-1} \\ P(k) = \left[I - K(k)\varnothing^T(k)\,\right]P(k) \end{cases} \tag{5}$$

In Eq. (5), $\hat{\theta}$ is the estimated parameter vector, K is the Kalman gain function, P is the error covariance coefficient, and I is the unit matrix. The initial values of the LMRLS method are taken from the parameter estimation results obtained by the RLS algorithm. The output at time step k is calculated using the result (initial value) obtained by the iter-ation at time step $k-1$ and the L + 1 set of data corresponding to the time steps $k-L$ to k. The iterative calculation process is shown in Eq. (6).

$$\begin{cases} \widehat{\theta}(k-L,k) = \widehat{\theta}(k-L,k-1) + K(k-L,k)\left[y(k) + \varnothing^T(k)\widehat{\theta}\left(k-L\,,k-1\right)\right] \\ K(k-L,k) = P(k-L,k-1)\varnothing(k)\left[\varnothing^T(k)P\left(k-L\,,k-1\right)\varnothing(k) + 1\,\right]^{-1} \\ P(k-L,k) = \left[I - K(k-L,k)\varnothing^T(k)\,\right]P(k-L,k-1) \end{cases} \tag{6}$$

In Eq. (6), L is the memory length. A set of data at time step k is added, and a set of data at time step $k-L$ is removed to maintain the memory length L as a constant value. Based on the L sets of data corresponding to the time steps $k-L+1$ to k and the results obtained from Eq. (5), the final solution formula of the LMRLS method at time step k is obtained, as shown in Eq. (7).

$$\begin{cases} \widehat{\theta}(k-L+1,k) = \widehat{\theta}(k-L,k-1) + K(k-L+1,k)\left[y(k-L) + \varnothing^T(k-L)\widehat{\theta}\left(k-L\,,k-1\right)\right] \\ K(k-L+1,k) = P(k-L,k-1)\varnothing(k-L)\left[\varnothing^T(k-L)P\left(k-L\,,k-1\right)\varnothing(k-L) + 1\,\right]^{-1} \\ P(k-L+1,k) = \left[I - K(k-L+1,k)\varnothing^T(k-L)\,\right]P(k-L,k-1) \end{cases} \tag{7}$$

Based on the electrical characteristic state-space description in Eq. (1), the Laplace transform is applied, as shown in Eq. (8).

$$U_T(s) = U_{oc}(s) - I_L(s)\left(R_0 + \frac{R_{p1}}{1+\tau_1(s)} + \frac{R_{p2}}{1+\tau_2(s)}\right) \tag{8}$$

In Eq. (8), s is the Laplace operator, $\tau_1 = C_{p1}R_{p1}$, and $\tau_2 = C_{p2}R_{p2}$. Then, the time constant variables are mathematically expressed, as shown in Eq. (9).

$$\begin{cases} a = \tau_1\tau_2 \\ b = \tau_1 + \tau_2 \\ c = R_0 + R_{p1} + R_{p2} \\ d = \tau_2\left(R_0 + R_{p1}\right) + \tau_1\left(R_0 + R_{p2}\right) \end{cases} \tag{9}$$

Substituting the time constant variables in Eq. (9), Eq. (8) is trans-formed into Eq. (10).

$$\frac{U(s)}{I_L(s)} = \frac{aR_0s^2 + ds + c}{as^2 + bs + 1} \tag{10}$$

In Eq. (10), $U(s) = U_T(s) - U_{OC}$. The function is transformed from the s to z domain using the bilinear transformation to ensure the consistent stability of the system before and after the transformation, as shown in Eq. (11).

$$s = \frac{2}{T_s}\frac{1 - z^{-1}}{1 + z^{-1}} \tag{11}$$

Eq. (11) is substituted into Eq. (10), which is simplified to obtain the discrete transfer function of the system. Then, MATLAB solves the transition from the s domain to produce a bilinear z domain trans-formation function, as shown in Eq. (12).

$$\frac{U(z^{-1})}{I_L(z^{-1})} = -\frac{\theta_3 + \theta_4z^{-1} + \theta_5z^{-2}}{1 - \theta_1z^{-1} - \theta_2z^{-2}} \tag{12}$$

The expressions of θ_1~θ_5 are calculated, as shown in Eq. (13).

$$\begin{cases} \theta_1 = -\dfrac{bT + 2a}{a + bT + T^2} \\ \theta_2 = \dfrac{a}{a + bT + T^2} \\ \theta_3 = \dfrac{cT^2 + dk + aR_0}{a + bT + T^2} \\ \theta_4 = -\dfrac{dT + a2R_0}{a + bT + T^2} \\ \theta_5 = \dfrac{aR_0}{a + bT + T^2} \end{cases} \tag{13}$$

The discrete recurrence equation of the voltage U_k is calculated using Eq. (14).

$$U_k = \theta_1U_{k-1} + \theta_2U_{k-2} + \theta_3I_k + \theta_4I_{k-1} + \theta_5I_{k-2} = \theta_kh_k^T \tag{14}$$

In Eq. (14), $\theta_K = [\theta_1, \theta_2, \theta_3, \theta_4, \theta_5]^T$, and $h_K = [U_{k-1}, U_{k-2}, I_k, I_{k-1}, I_{k-2}]^T$. Where θ_K is the parameter vector that needs to be identified for the battery system, and h_K is the information vector made up of input and output datasets.

Consequently, a VFF-LMRLS method is proposed to identify the battery model parameters based on the LMRLS algorithm. The VFF- LMRLS method divides its recursive equation into segments based on receiving new input data and eliminating old data, which are expressed in Eqs. (15) and (16), respectively. The receiving of new input data is expressed, as shown in Eq. (15).

$$\begin{cases} e(k+L) = y(k+L) - h^T(k+L)\widehat{\theta}(k,k-1+L) \\ \lambda(k+L) = 1 - \dfrac{e^2(k+L)}{1 + h(k-1+L)P(k,k-1+L)h^T(k-1+L)} \\ K(k,k+L) = \dfrac{P(k,k-1+L)h(k+L)}{\lambda(k+L) + h(k+L)P(k,k-1+L)h^T(k+L)} \\ \widehat{\theta}(k,k+L) = \widehat{\theta}(k,k-1+L) + K(k,k+L)e(k+L) \\ P(k,k+L) = \dfrac{I - K(k,k+L)h^T(k+L)P(k,k-1+L)}{\lambda(k+L)} \end{cases} \tag{15}$$

Therefore, removing old data allows for the elimination of data saturation, as shown in Eq. (16).

$$\begin{cases} e(k+1+L) = y(k+1+L) - h^T(k+1+L)\widehat{\theta}(k+1,k+L) \\ \lambda(k+1+L) = 1 - \dfrac{e^2(k+1+L)}{1+h(k+1+L)P(k,k+L)h^T(k+1+L)} \\ K(k+1,k+L) = \dfrac{P(k,k+L)h(k+1+L)}{\lambda(k+1+L)+h(k+1+L)P(k,k+L)h^T(k+1+L)} \\ \widehat{\theta}(k+1,k+L) = \widehat{\theta}(k,k+L) + K(k+1,k+L)e(k+1+L) \\ P(k+1,k+L) = \dfrac{I-K(k+1,k+L)h^T(k+1+L)P(k,k+L)}{\lambda(k+1+L)} \end{cases} \tag{16}$$

In Eqs. (15) and (16), $\lambda(k + L)$ or $\lambda(k + 1 + L)$ is the equation used to update the variable forgetting factor. The characteristic micro-parameters of the established battery state estimation method to be identified, as well as the characteristic internal ohmic resistance $R_0(k)$ of the system, are shown in Eq. (17).

$$\begin{cases} R_0(k) = \dfrac{\widehat{\theta}_3(k) - \widehat{\theta}_4(k) + \widehat{\theta}_5(k)}{1+\widehat{\theta}_1(k) - \widehat{\theta}_2(k)} \\ R_{p1}(k) = \dfrac{R_0(k)\tau_2(k) + c(k)\tau_1(k) - d(k)}{\tau_1(k) - \tau_2(k)} \\ R_{p2}(k) = \dfrac{d(k) - R_0(k)\tau_1(k) - c(k)\tau_2(k)}{\tau_1(k) - \tau_2(k)} \\ C_{p1}(k) = \dfrac{\tau_1(k)}{R_{p1}(k)} \\ C_{p2}(k) = \dfrac{\tau_2(k)}{R_{p2}(k)} \end{cases} \tag{17}$$

Using the VFF-LMRLS method, the accurate micro-parameters of the dynamic migration battery models are then obtained.

2.3. Enhanced EEMDA-DEKF method for SOC and SOH co-estimation

2.3.1. Dual extended Kalman filter method for SOC and SOH co-estimation

The EKF method linearizes the nonlinearities of lithium-ion batteries by applying partial derivatives and first-order Taylor series expansion to the system state-space equation. It is a better regression data processing algorithm than the traditional KF method, but it only estimates with first-order accuracy [63]. It estimates the current time step's state value based on the estimation and observation of the previous and current time steps, respectively.

Since the SOC and SOH have coupling effects and it is challenging to accurately estimate the actual state of the battery by estimating just one state, the DEKF in this study is used to achieve the synergistic estimation of the SOC and SOH. The DEKF method employs two EKFs, the first of which estimates the SOC of the battery and the second of which simultaneously estimates the capacity by updating the control-input matrix in the state-space equation. When estimating the SOC, the bat-tery capacity is treated as the only state variable and the SOC as a constant, and vice versa when estimating the capacity. In the separate estimation of SOC, the Q in the control-input matrix is the calibrated capacity value, which does not change when the number of iterations increases. Q is inversely updated and adjusted during the co-estimation to account for the mutual optimization and effects of the two-state pa-rameters. To achieve a synergistic estimation of the SOC and capacity of the battery, the ampere-hour integral equation is used as a connection between the two-state parameters. The working principle of the DEKF method is shown in Table 1.

In Table 1, H_Q is the coefficient of the measurement matrix for bat-tery capacity estimation. R_k and Q_k denote the associated with the system process noise and the observation noise, respectively. The difference between the observed value and the estimated value of EKF1 and EKF2 is expressed by yk+1 ŷk+1|k and yQ,k+1 ŷQ,k+1|k, respectively. Ak, Bk, and Ck denote the state transition, control-input matrix, and measurement matrices, respectively, for SOC estimation, whose expressions are pre-sented in Eq. (18).

2.3.2. Ensemble empirical mode decomposition method with adaptive noise

An adaptive signal processing method to analyze nonlinear and non- stationary time sequences, the EMD, has been extensively used [64]. Since the EMD is highly adaptable, setting up basis functions and workable decomposition layers is not necessary. Through step-by-step decomposition, the EMD method transforms battery input data into components of various frequencies known as intrinsic mode functions (IMFs) and residual energy [65]. The original input signals are divided by the EMD into several IMFs, each of which contains unique data on different time-frequency scales. When utilizing the EMD, the following conditions must be satisfied: (1) The numbers of extrema and zero crossings must be equal or differ from one another by no more than one. (2) The mean value of the encoder, which is derived from local maxima and minima, should be zero at all times, i.e., the encoding must be symmetric on zero. Using the original signal, the reconstructed sum of the intrinsic mode functions is expressed in Eq. (19).

Table 1
The working principle of the DEKF method.

EKF1 for SOC estimation based on battery parameters
Step 1: Parameter initialization $\begin{cases} \widehat{x}_0 = E(x_0) \\ P_0^x = E\left[(x_0 - \widehat{x}_0)(x_0 - \widehat{x}_0)^T\right] \\ \widehat{Q}_0 = E(Q_0) \\ P_0^Q = E\left[(Q_0 - \widehat{Q}_0)(Q_0 - \widehat{Q}_0)^T\right] \end{cases}$ Step 2: Time update Priori state estimation: $\widehat{x}_{k\|k-1}^- = A_k x_{k-1}^- + B_k u_{k-1}^+ + R_{k-1}$ Priori error covariance matrix: $P_k^- = A_k P_{k-1}^+ A_k^T + Q_{k-1}$ Step 3: Measurement update Kalman gain matrix: $K_k = P_k^- H_k^T [H_k P_k^- H_k^T + R_k]^{-1}$ Posteriori state estimation: $\widehat{x}_{k+1}^+ = \widehat{x}_k^- + K_k(y_k - \widehat{y}_k)$ Posteriori error covariance matrix: $P_{k+1\|k}^+ = (I - K_k H_k) P_k^- + Q_k$
EKF2 for SOH value calculation based on estimated capacity
Priori state and error covariance update of capacity: $\begin{cases} \widehat{Q}_{k\|k-1} = \widehat{Q}_{k\|k} \\ P_{Q,k\|k-1} = P_{Q,k\|k} + R_k \end{cases}$ Calculate the Kalman gain: $K_{Q,\ k+1} = P_{Q,\ k\ \|k} H_{Q,\ k+1}^T [H_{Q,\ k+1} P_{Q,\ k\ \|k} H_{Q,\ k+1}^T + R_{Q,\ k}]^{-1}$ Posteriori state and error covariance update of capacity: $\begin{cases} \widehat{Q}_{k+1\|k} = \widehat{Q}_{k+1\|k} + K_{Q,k+1}(y_k - \widehat{y}_k) \\ P_{Q,k+1\|k} = (I - K_{Q,k+1} H_{Q,k+1}) P_{Q,k\ \|k} + Q_k \end{cases}$

$$A_k = \begin{bmatrix} 1 & 0 & 0 \\ 0 & exp\left(-\dfrac{\Delta k}{C_{p1} R_{p1}}\right) & 0 \\ 0 & 0 & exp\left(-\dfrac{\Delta k}{C_{p2} R_{p2}}\right) \end{bmatrix}$$

$$B_k = \begin{bmatrix} -\eta \cdot \Delta k / Q_n \\ R_{p1}\left(1 - exp\left(-\dfrac{\Delta k}{C_{p1} R_{p1}}\right)\right) \\ R_{p2}\left(1 - exp\left(-\dfrac{\Delta k}{C_{p2} R_{p2}}\right)\right) \end{bmatrix} \tag{18}$$

$$C_k = \begin{bmatrix} \dfrac{dU_{oc}}{dSOC_k} & -1 & -1 \end{bmatrix}$$

$$x(k) = \sum_{i=1}^{N} f_i(k) + r(k) \tag{19}$$

In Eq. (19), N is the number of IMFs, r is the residual, which repre-sents the overall trend of the input signal. It is worth noting that as subscript i increases, the f_i denotes the IMFs, which reflect the frequency characteristics of the original signal from high to low. The IMFs component reflects the process of capacity regeneration, and the residual component reflects the true battery state.

The noise-assisted data analysis method, used by the EEMD, which adds white noise of finite amplitude before EMD in each trial, is proposed as a solution to this problem. The ensemble average of trials is then used to define the actual IMF. The ensemble average is also used to remove the white noise that was added to the original data because it is independent of the trials. True IMFs can be extracted more readily because the EEMD lessens the mode mixing effect. However, the noise elimination procedure is time-consuming. Additionally, using various white noises will result in different modes. Hence, the high computational cost and randomness of the final results limit its applications. An improvement to the spectral separation of the IMFs and a precise reconstruction of the original signal is provided by the EEMD with an adaptive noise method, which can be summed up as follows:

The input signal $x(k)$ is combined with a Gaussian white noise $\varepsilon_0 w_i(k)$ to create the output signal $y(k)$, which is then decomposed using EMD to yield the first $f_i(k)$ component, as shown in Eq. (20).

$$\begin{cases} y(k) = \varepsilon_0 w_i(k) + x(k) \\ f_i(k) = \dfrac{1}{I}\sum_{i=1}^{N} f_1^i(k) \end{cases} \tag{20}$$

In Eq. (20), ε_0 denotes the amplitude of the added noise. The Gaussian white noise with unit variance is represented by $w_i(k)$. Then, the first residual after the first staged decomposition is computed, as shown in Eq. (21).

$$r_k = y(k) + f_i(k) \tag{21}$$

The second mode, $f_2(k)$, is obtained by decomposing each $r_k + \varepsilon_i E_i(w_i(k))$ by the EMD, as shown in Eq. (22).

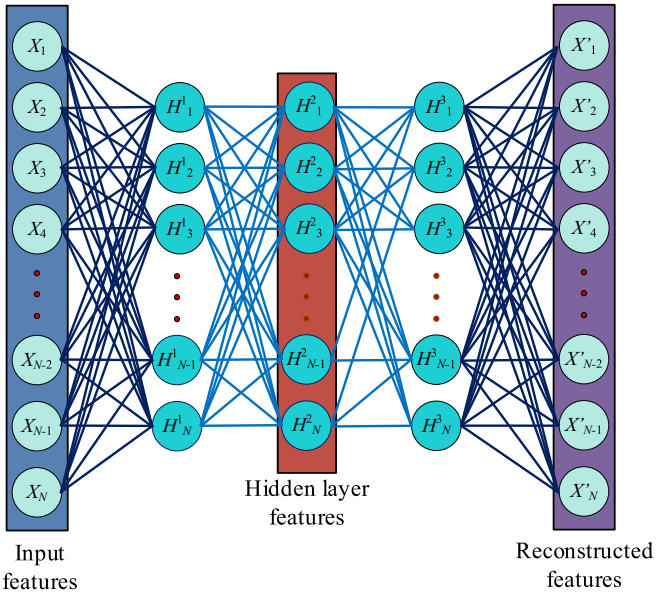

Fig. 2. The multi-layered and -purpose autoencoder.

$$f_2(k) = \frac{1}{I}\sum_{i=1}^{N} E_1(r_k + \varepsilon_1 E_1(w_i(k))) \tag{22}$$

In Eq. (22), $E(\cdot)$ denotes the function used to extract the IMF decomposed by the EMD. For k = 2, …, Nk, the kth residual is computed, as shown in Eq. (23).

$$r_k = r_{k-1}(k) - f_i(k) \tag{23}$$

Then, each computed residual $r_k + \varepsilon_k E_k(w_k(k))$ is decomposed by the EMD, the k + 1th mode f_{k+1} is obtained, as shown in Eq. (24).

$$f_k(k) = \frac{1}{I}\sum_{i=1}^{N} E_1(r_k + \varepsilon_k E_k(w_i(k))) \tag{24}$$

Finally, Eqs. (23) and (24) are repeated until the output of the re-sidual r_k is constant.

2.3.3. Multi-functional autoencoding method

A fully connected symmetric neural network with two parts, an encoder, and a decoder, make up the autoencoder. With the help of this neural network, unsupervised learning is made possible with the goal of producing reconstructed features with a dimension identical to the original input data [66]. In this paper, the autoencoder is employed for multi-functional purposes by receiving, reconstructing, and outputting the decomposed features from the EEMD for the DEKF method to esti-mate the SOC and SOH of the battery.

First, using the feature-extracted input data $x_e \in \mathbb{R}^N$, the encoded latent feature. The decoded reconstruction output feature is shown in Eq. (25).

$$\begin{cases} h(x_e) = \sigma(w_e x_e + b_e) \\ \hat{x}_e = \sigma(w_d z + b_d) \end{cases} \tag{25}$$

In Eq. (25), $h(x_e)$ represents the encoder activation vector, $\hat{}x_e \in \mathbb{R}^N$ represents the estimated output vector, and σ represents a nonlinear activation function. $w_e \in \mathbb{R}^{N\times M}$ and $w_d \in \mathbb{R}^{M\times N}$ represent the weight matrices of the encoder and decoder, respectively. Also, b_e and b_d represent the bias vectors of the encoder and decoder, respectively.

Therefore, the weights of the parameters $\varnothing = \{w_e, w_d, b_e, b_d\}$ are updated to minimize a reconstruction error of $R(x_e, \hat{x}_e)$ based on a least- squares loss function, as shown in Eq. (26).

$$\begin{cases} \widehat{\varnothing}_{rec} = argmin \sum_{i=1}^{N} R(x_e, \hat{x}_e) \\ R(x_e, \hat{x}_e) = x_{ei}(i) - \hat{x}_{ei}(i) \end{cases} \tag{26}$$

In this paper, the autoencoder used comprises four layers, two each in the encoder and decoder, as shown in Fig. 2.

The multi-dimensional extracted-feature inputs are condensed into six- and four-dimensional features at each layer of the encoder. Four-dimensional data are further decoded into six-and nine-dimensional features with the same dimension as the input data at the end of each decoder layer. Each layer's hidden nodes are trained to reduce the amount of reconstruction error between the features that were reconstructed and the outliers that are removed. The exponential linear unit function is additionally added at each layer to take into account the nonlinear aspects of degradation. Since the feature spaces are condensed through linear space transformation, an autoencoder without a nonlinear activation function is typically comparable to the principal component analysis. The unsupervised learning process of feature reconstruction effectively reduces the variations in several extracted features and successfully extracts the long-term degradation trends from noise.

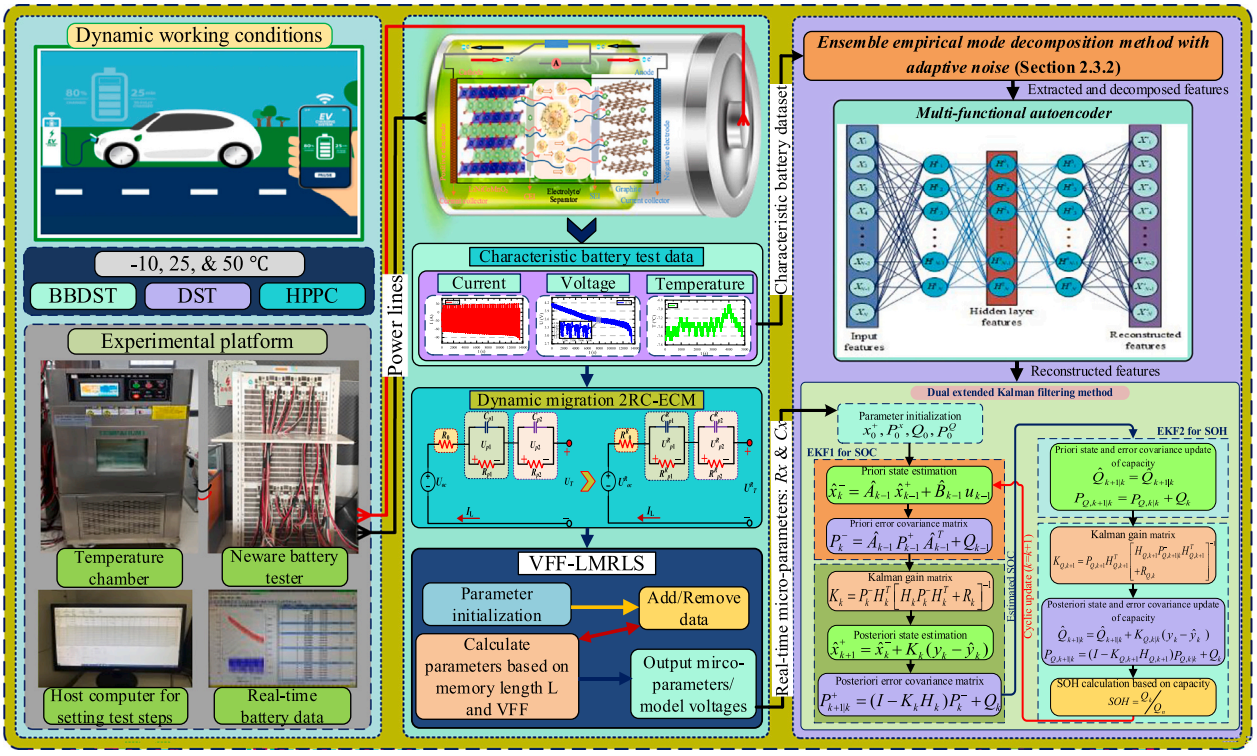

Fig. 3. The flowchart of the multi-state estimation methods.

Table 2
The fundamental technical details of the ternary lithium-ion battery.

Parameter		Value
Nominal capacity		70 Ah
Nominal voltage		3.7 V
Charge	Cutoff voltage	4.2 V
	Standard current	1 C
Discharge	Cutoff voltage	2.75±0.05 V
	Standard current	3 C
Working temperatures		−20–60 °C
Dimension (l × w × h)		148 × 33 × 93 (mm)

2.4. Architectural framework for SOC and SOH co-estimation

The SOC and SOH co-estimation method study consists of four parts, namely: (1) The real-time battery tests at temperatures of − 10, 25, and 50 °C under complex working conditions; (2) The online VFF-LMRLS parameter identification method based on the dynamic migration 2RC-ECM for micro-parameter estimation and model verification; (3) The EEMD with adaptive noise and an autoencoder for feature extraction, decomposition, and reconstruction; and (4) The optimal SOC and SOH co-estimation using the proposed EEMDA-DEKF method. The schematic diagram is presented in Fig. 3.

After the dynamic migration 2RC-ECM battery model's ability to track the closed-circuit voltage is verified, its micro-parameters are estimated using VFF-LMRLS for the DEKF and the proposed EEMDA- DEKF methods to co-estimate the SOC and SOH. A comparative study using the error metrics is conducted to critically evaluate the perfor-mance of each method, as presented in the following section.

2.5. Battery state parameter evaluation criteria

In this paper, three evaluation metrics are used to measure the ac-curacy of the battery model performance, micro-parameter estimation, and state estimation of the proposed methods: the maximum error (ME), the mean absolute error (MAE), and the root mean square error (RMSE). Their mathematical calculations are described in Eq. (27).

$$\begin{cases} E_k = y_k - \widehat{y}_k \\ ME = max1, 2, \ldots, N|E_k| \\ MAE = \dfrac{1}{N}\sum_{k=1}^{N}|E_k| \\ RMSE = \sqrt{\dfrac{1}{N}\sum_{k=1}^{N}(E_k)^2} \end{cases} \tag{27}$$

In Eq. (27), k is the non-missing data time step, N is the total length of the given data sample, and E_k is the estimated state parameter error value at time step k. y_k is the actual state parameter value of the battery system and $\hat{y}_k$ is the estimated state parameter value by the proposed method at time step k.

3. Experimental battery and testing conditions

In this paper, the research object is a ternary lithium-ion battery with a rating of 70 Ah and a nominal voltage of 3.7 V. The anode of the cell is made of graphite, and the cathode is made of lithium nickel cobalt manganese oxide ($LiNiCoMnO_2$). The fundamental technical details of the ternary lithium-ion battery are presented in Table 2.

As shown in Fig. 3, a host computer is responsible for setting different complex working conditions and logging voltage, current, and other data about the battery. Information about the operational condition's effects on the battery is recorded using the experimental platform, and the retrieved data are the voltage, current, capacity, etc., at a time in-terval of 0.1 s. The data is transferred between the two devices using the TCP/IP cable, and the high-power battery tester regulates the battery's charge and discharge states.

The lithium-ion battery is placed in a temperature test chamber during its operation under various working conditions to study the temperature effects while connected to the charge-discharge test equipment through the power cable to ensure that the experimental condition temperatures are 10, 25, and 50 ◦C. To test and verify the efficacy of parameter identification and the superiority of the suggested co-estimation method, the Beijing bus dynamic stress test (BBDST), dynamic stress test (DST), and hybrid pulse power characterization (HPPC) working conditions are adopted in the experiment in this paper. The working steps and characteristic data curves at 10, 25, and 50 ◦C under the BBDST, DST, and HPPC working conditions can be found in [3,26].

4. Results and discussion

4.1. Battery model verification and micro-parameter estimation

4.1.1. Established battery model verification

At 25 °C, the 2RC-ECM's inherent accuracy limitation is evaluated and selected as a benchmark to verify the performance of the proposed dynamic migration 2RC-ECM in precisely identifying the parameters of the ECM under BBDST, DST, and HPPC working

conditions. The closed- circuit voltage error curves are then obtained by subtracting the battery's closed-circuit voltage outputs simulated by the battery models using the actual terminal voltage from the battery, as shown in Fig. 4.

In Fig. 4, it can be observed that the dynamic migration battery model can accurately characterize the nonlinear changes of the battery more effectively than the conventional 2RC-ECM. It can be observed that, under the BBDST, DST, and HPPC working conditions, the conventional 2RC-ECM has maximum output error values of 17.899 V, 12.391 V, and 6.78 V, respectively. Meanwhile, the dynamic migration 2RC-ECM has maximum output error values of 9.289 V, 5.922 V, and 3.973 V, respectively. These results signify a performance improvement of 48.10%, 52.21%, and 41.40%, respectively. Even though at the end of discharge, the voltage error tends to increase, such in-depth charge depletion is rarely experienced in real-time due to the intention to protect the battery. The dynamic migration battery model effectively reduces the noise and eliminates the large errors during the traction processes with highly stable traction characteristics. Thus, it validates that the parameterized model adequately captures the electrical dy-namics of the lithium-ion battery, serving as a strong foundation for the model-based state estimation method.

Furthermore, the MAE and RMSE metrics are used to critically evaluate the performance of the dynamic migration 2RC-ECM compared to the conventional 2RC-ECM, as shown in Table 3.

In Table 3, it can be observed that the dynamic migration 2RC-ECM has lower MAE and RMSE values compared to the conventional 2RC-ECM. These findings demonstrate that, when compared to the conventional 2RC-ECM, the dynamic migration 2RC-ECM provides much more accuracy in adequately characterizing the nonlinearities of the lithium-ion battery. The dynamic migration battery model application provides a strong framework for more accurately completing the SOC and SOH co-estimation of lithium-ion batteries.

4.1.2. Characteristic micro-parameter estimation

The battery's ability to produce a certain amount of power is closely related to its impedance characteristics. It describes the voltage across the battery caused by the application of current. It depends significantly on the battery's SOC, temperatures, charge-discharge current rates, cyclic depth, and lifetime aging [67]. The dynamically varying curves for the experimental findings of the internal ohmic resistance and polarization resistances and capacitances at different temperatures are pre-sented in Fig. 5.

Fig. 5 illustrates the dependency of the temperature on the internal ohmic and polarization resistances and capacitances at different temperatures. It can be observed that the ohmic resistance (R_0) relationship to temperature is very high at −10 °C, moderately high at 50 °C, and stable at 25 °C. Furthermore, it can also be observed that the electro-chemical and concentration polarization resistances (R_{p1} and R_{p2}) are high at −10 °C while those at 25 and 50 °C remain moderate and low, respectively. This is because the impedance is dominated by the electrolyte and increases with decreasing temperature [67]. Furthermore, it can be observed that the electrochemical and polarization capacitances (C_{p1} and C_{p2}) are approximately opposite to the resistances, where at 50 °C, both capacitances show an increasing trend with discharging time. Meanwhile, at temperatures of −10 and 25 °C, these parameters remain almost constant, exhibiting nearly identical trends. This is because it is generally known that the absolute value of this double capacitance increases over the lifetime of the battery and is not so much dependent on temperature [67,68], which is also again in agreement with the results presented in this paper.

4.2. SOC-SOH co-estimation under various temperatures and working conditions

Using the VFF-LMRLS method established based on the dynamic migration 2RC-ECM, the experimental verification of SOC and SOH co-estimation of the proposed EEMDA-DEKF method is conducted under the BBDST and DST working conditions. For the SOH estimation, the reference values of 96.42%, 99.83%, and 97.95% at temperatures of −10, 25, and 50 °C, respectively, are obtained through rigorous capacity determination tests. The battery is fully charged and discharged three times to determine its actual capacity in the current state and to calculate the current SOH levels.

4.2.1. Co-estimations under the BBDST working condition

In addition to the basic working conditions such as starting, braking, and stopping, the BBDST also includes acceleration, taxiing, and rapid acceleration, which are acquired from actual data collected during the operation of the Beijing bus. The SOC and SOH co-estimation results of the DEKF and EEMDA-DEKF methods under the BBDST working condition are shown in Fig. 6.

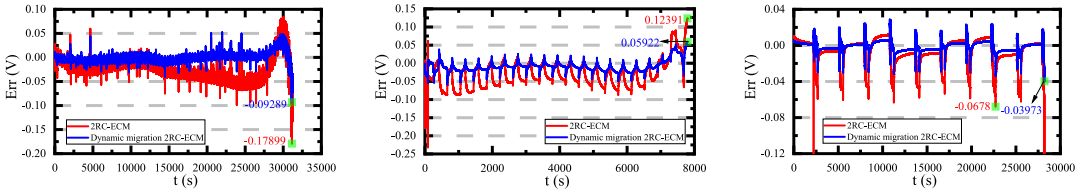

(a) BBDST working condition (b) DST working condition (b) HPPC working condition

Fig. 4. Comparison of closed-circuit voltage traction errors for different battery models.

Table 3
Comparative traction analysis of the battery models.

Battery model	BBDST		DST		HPPC	
	MAE	RMSE	MAE	RMSE	MAE	RMSE
Conventional 2RC-ECM	2.6809%	3.1639%	4.0899%	4.8684%	1.2083%	2.1441%
Dynamic migration 2RC-ECM	0.6052%	1.0036%	1.4394%	1.7515%	0.4007%	0.5381%

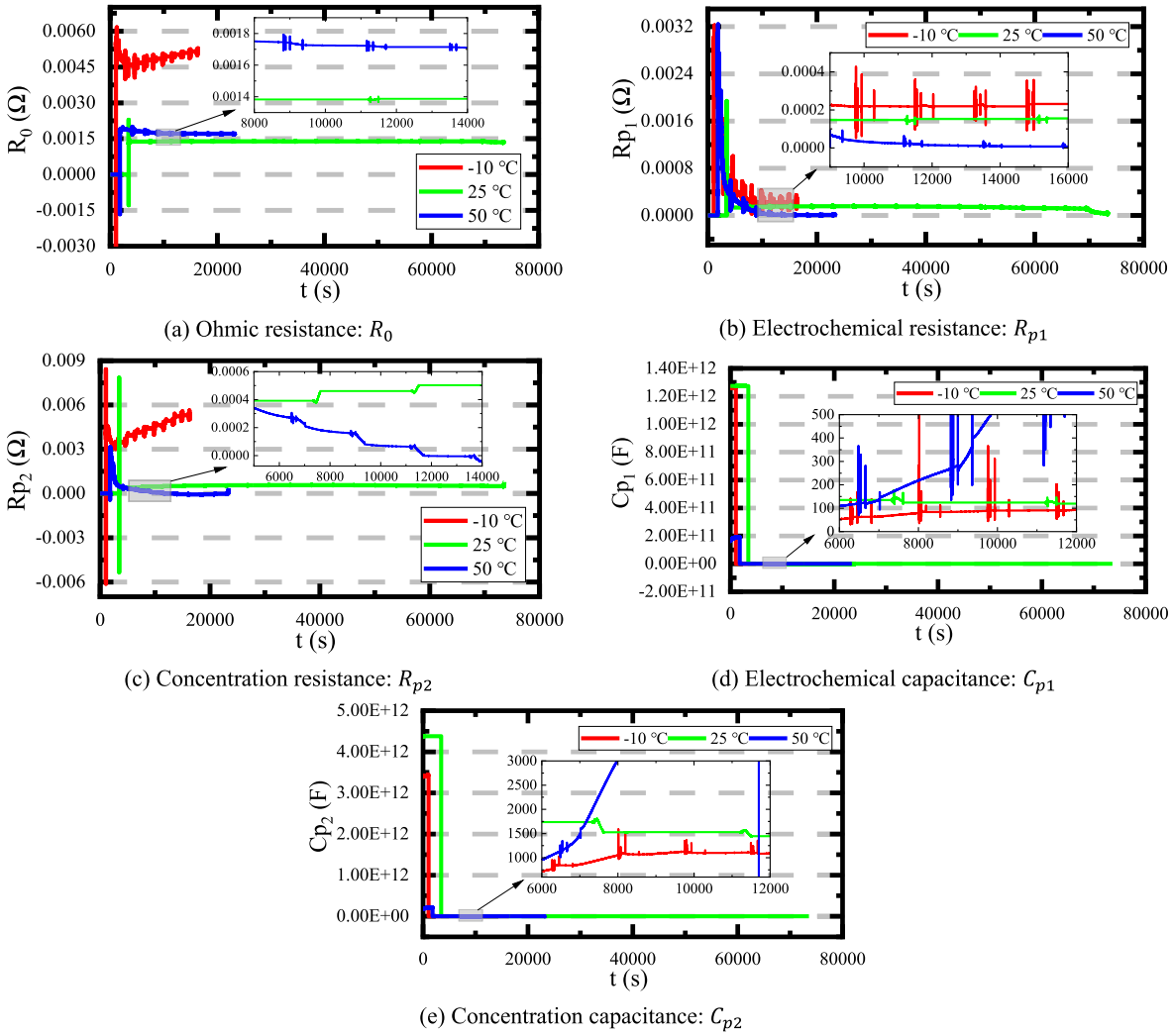

Fig. 5. Dynamics of the characteristic micro-parameters estimated at different temperatures under the HPPC working condition.

As can be observed from Fig. 6, the SOC and SOH estimation results for the DEKF and the proposed EEMDA-DEKF method show that the proposed method is highly optimal for BMS application. For the SOC estimation results, it can be observed that the DEKF method fluctuates greatly and is extremely unstable. It has ME values of 0.685%, 0.426%, and 0.948% at temperatures of −10, 25, and 50 °C, respectively. Then, its SOH estimation results show it has ME values of 1.437%, 5.414%, and 1.965%, respectively. Meanwhile, the proposed EEMDA-DEKF method estimates the SOC with ME values of 0.211%, 0.137%, and 0.523% at temperatures of −10, 25, and 50 °C, respectively. Additionally, its SOH estimation results show that it has ME values of 0.0517%, 1.327%, and 0.366%, respectively.

Furthermore, it can be observed that the estimations by the proposed EEMDA-DEKF method have greatly improved as a whole. Even when operating under the dynamic BBDST working condition, it maintains high stability. The method has a very high level of robustness, and the estimation results do not change significantly due to the ability of the EEMD to extract and decompose the IMF for the autoencoder to reconstruct the features for accurate multi-state estimations.

4.2.2. Co-estimations under the DST working condition

Under the DST working condition, the correlated estimations and analyses are performed to ensure accurate estimation of the states of the battery in real-time applications. The SOC and SOH co-estimation results are shown in Fig. 7.

The SOC and SOH co-estimation results are conducted at different temperatures under the DST working condition, as shown in Fig. 7. Compared to the DEKF method, the proposed EEMDA-DEKF method enhances the accuracy of the estimates significantly when the battery's temperature changes considerably. At temperatures of −10, 25, and 50 °C, the DEKF method estimates the SOC with ME values of 4.556%, 1.983%, and 2.021%, respectively. At the same time, it estimates the SOH with ME values of 3.005%, 0.4882%, and 2.304%, respectively. However, when it comes to the proposed EEMDA-DEKF method, the ME values for the SOC estimations are 0.4872%, 0.117%, and 0.559%. Meanwhile, for the estimation of the SOH, it has ME values of 0.3751%, 0.1998%, and 0.192%, respectively.

Considering varying temperatures and working conditions over the entire battery lifecycle, it can be observed that the undesirable battery state estimation effects that negatively impact the DEKF method and result in inaccuracies, fluctuation, etc., are corrected and optimized by the EEMDA-DEKF method. This is due to the feature extraction, decomposition, and reconstruction by the EEMDA proposed for the conventional DEKF method, which has optimal performance at a temperature of 25 °C.

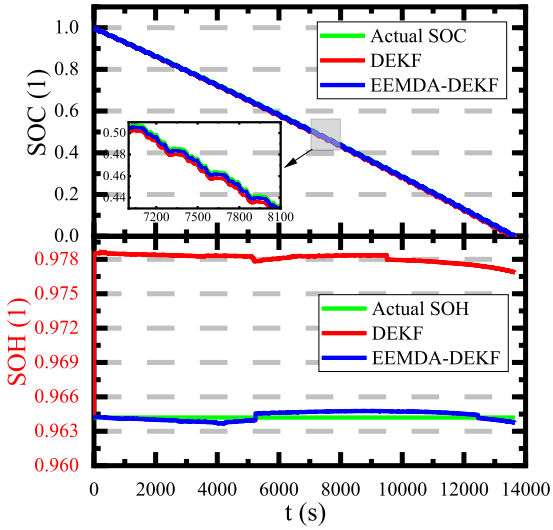

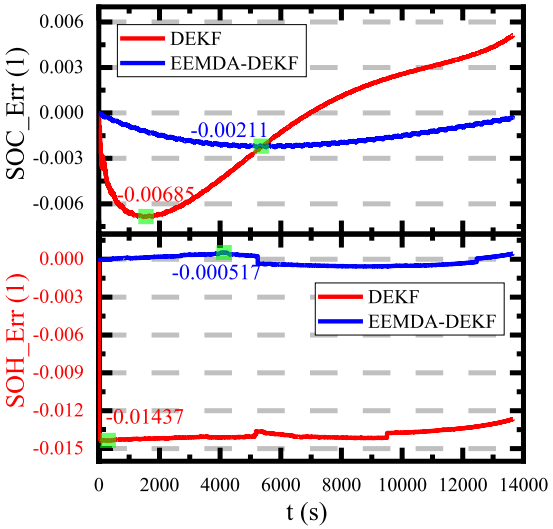

(a) Co-estimation and error curves at -10 °C

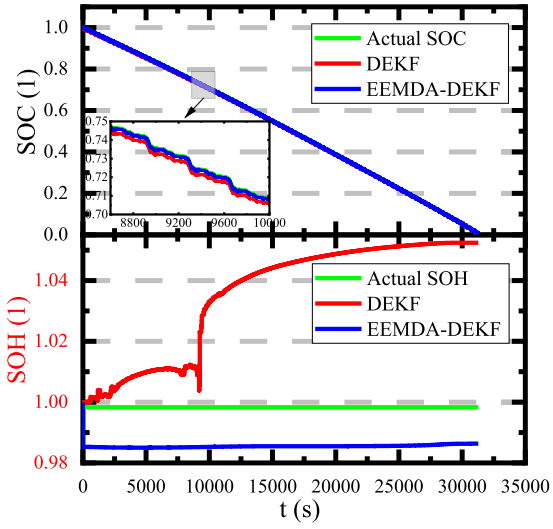

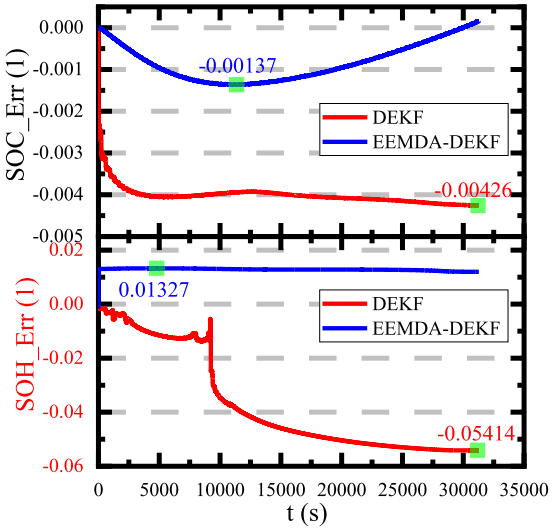

(b) Co-estimation and error curves at 25 °C

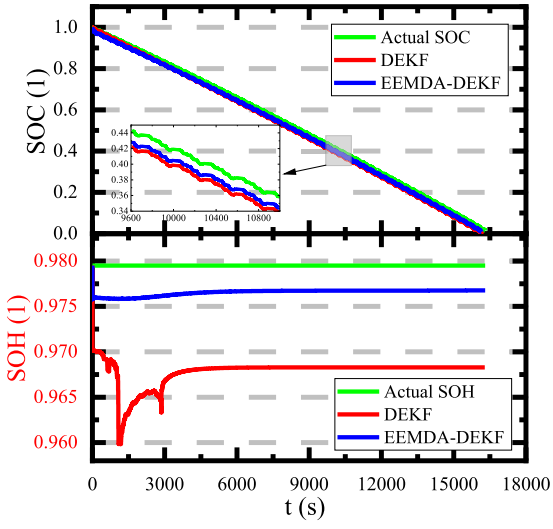

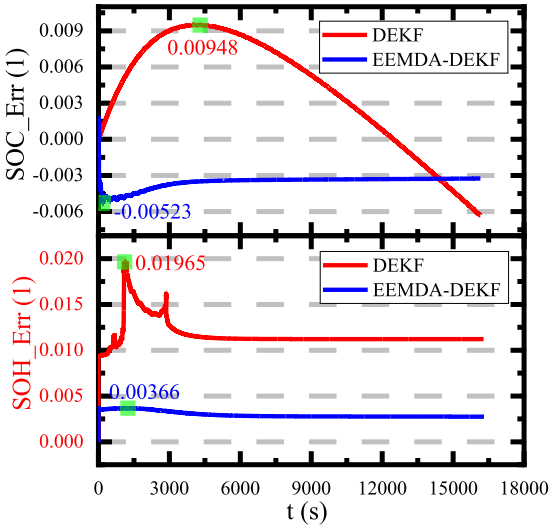

(c) Co-estimation and error curves at 50 °C

Fig. 6. SOC-SOH estimation and error results under the BBDST working condition.

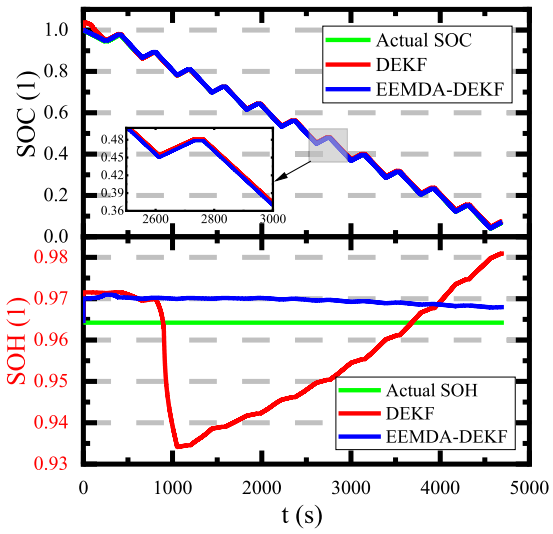

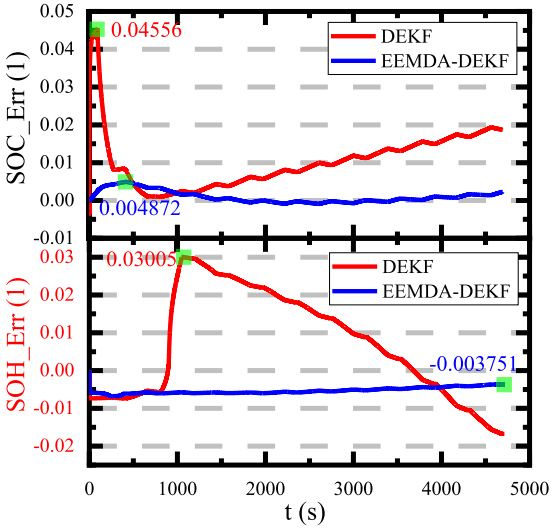

(a) Co-estimation and error curves at -10 °C

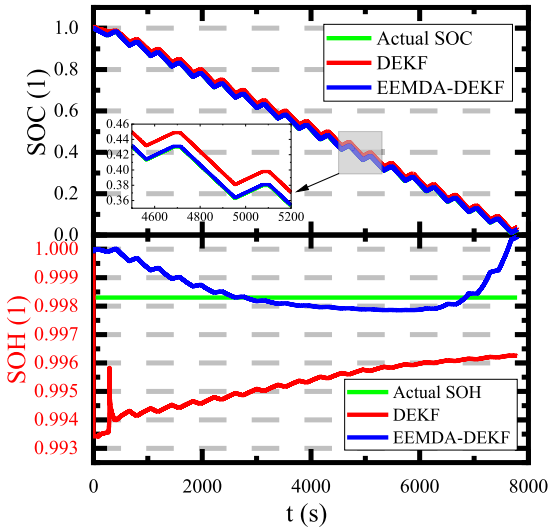

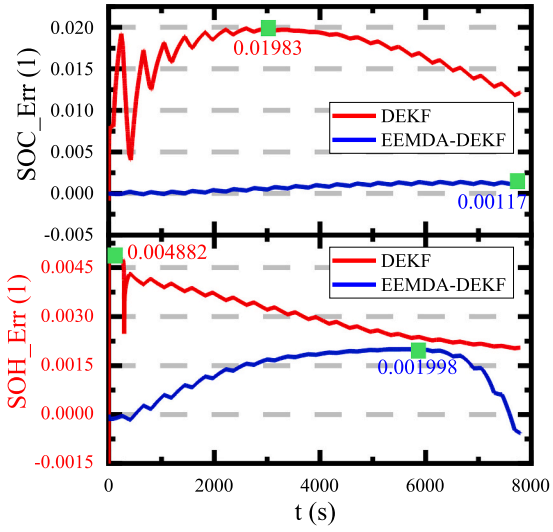

(b) Co-estimation and error curves at 25 °C

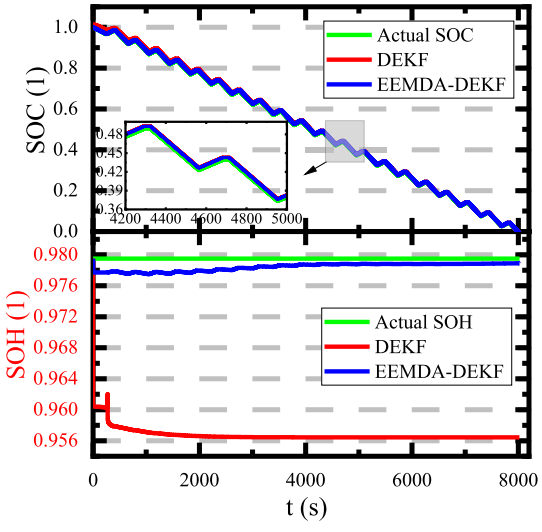

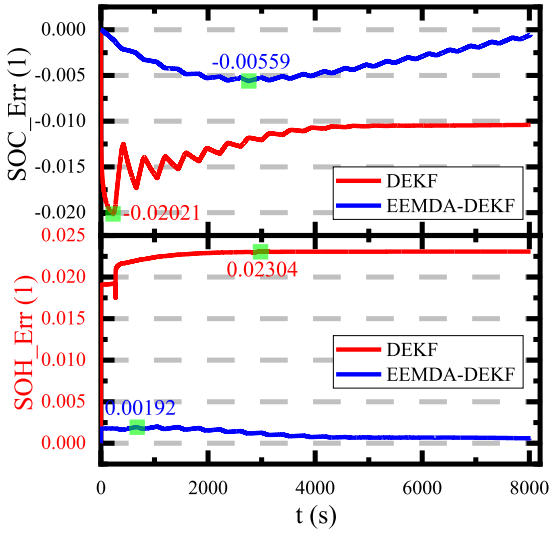

(c) Co-estimation and error curves at 50 °C

Fig. 7. SOC-SOH estimation and error results under the DST working condition.

Table 4
The quantitative evaluation of the SOC and SOH estimation performances.

Working conditions	Operating temperatures	SOC-SOH co-estimation methods			
		DEKF		EEMDA-DEKF	
		MAE	RMSE	MAE	RMSE
SOC estimation evaluation					
BBDST	−10 °C	0.3456%	0.3975%	0.1523%	0.1635%
	25 °C	0.4017%	0.4024%	0.0831%	0.0939%
	50 °C	0.5362%	0.6142%	0.3520%	0.3568%
DST	−10 °C	1.0343%	1.2822%	0.1263%	0.1829%
	25 °C	1.6549%	1.6969%	0.0739%	0.0877%
	50 °C	1.3121%	1.3315%	0.4313%	0.4513%
SOH estimation evaluation					
BBDST	−10 °C	1.3882%	1.3897%	0.0362%	0.0396%
	25 °C	3.6848%	4.1351%	1.2827%	1.2831%
	50 °C	1.1669%	1.1762%	0.2961%	0.2977%
DST	−10 °C	1.3202%	1.5601%	0.5333%	0.5388%
	25 °C	0.2987%	0.3105%	0.1353%	0.1499%
	50 °C	2.2767%	2.2781%	0.1081%	0.1181%

Two major conclusions can be drawn from the experimental results in this section. First, compared to the conventional DEKF method, the proposed EEMDA-DEKF method offers adequate estimation perforfance at different temperatures. Even though its computational costs and complexities are a little higher compared to the DEKF method, the accuracy and robustness are significant for practical SOC and SOH estimation of lithium-ion batteries. Second, by utilizing the EEMDA method's capacity to extract, decompose, and reconstruct the extracted features from the battery input current, voltage, and temperature variables, the proposed DEKF method can co-estimate the SOC and SOH with sufficient accuracy under the various complex working conditions.

4.3. Performance analysis of the proposed method for SOC-SOH co-estimation

The MAE and RMSE metrics are used to compare the two methods to further verify the reliability and robustness of the proposed method. The numerical results of the DEKF and EEMDA-DEKF methods at different temperatures under the BBDST and DST working conditions for the quantitative analysis of the SOC and SOH estimation performances are presented in Table 4.

Lithium-ion batteries have strong nonlinear and time-varying prop-erties due to the complex electrochemical reaction processes, which are also influenced by environmental conditions. From Table 4, it can be observed that the SOC and SOH performance of the proposed EEMDA-DEKF method is optimal compared to the conventional DEKF method. The results show that the DEKF method has optimal MAE and RMSE values of 0.3456% and 0.3975%, respectively, for the SOC estimation. Comparatively, the proposed EEMDA-DEKF method also has 0.0233% and 0.0252%, respectively, for SOC estimation. At the same time, for the SOH performance evaluation, the results show that the conventional DEKF method has optimal MAE and RMSE values of 0.1063% and 0.1111%, respectively. Meanwhile, the proposed EEMDA-DEKF method has optimal MAE and RMSE values of 0.0362% and 0.0396%, respectively, at different temperatures under the BBDST and DST working conditions, which are optimal improvement values to ensure accurate SOC and SOH estimation for real-time BMS applications.

5. Conclusion and future work

In this paper, an EEMDA-DEKF method is proposed to achieve high-precision real-time SOC and SOH co-estimation of lithium-ion batteries. This method provides a more accurate estimate of the battery's remaining energy, which will benefit the users in determining how far the EV can be driven safely. First, battery tests are conducted at different temperatures under complex working conditions. Second, to ensure higher computational efficiency when mapping the model parameters to the states of the battery based on the dynamic migration 2RC-ECM for the DEKF method, a VFF-LMRLS method is established to identify the characteristic micro-parameters of the dynamic migration battery model online. The novelties of this paper are as follows: Based on the identified characteristic micro-parameters of the battery using the VFF-LMRLS method, the sensitivity analysis shows that internal resistances are the predominant parameter among all the model parameters, of which significant change occurs, especially at a temperature of − 10 °C. Furthermore, various characteristic micro-parameters at different temperatures provide significant insight into the dynamic changes during the operation of the battery. Besides, the internal resistance is shown to have potentially increased over the operation time, which may be beneficial for the battery's SOC and SOH evaluation. The proposed EEMDA methods provide the DEKF method with the relevant and reconstructed data features for the SOC and SOH co-estimation of the lithium-ion battery to guarantee reliability and stability for real-time applications. Using the proposed EEMDA-DEKF method, the experimental validation results demonstrate an MAE and RMSE performance improvement of 93.26% and 93.66%, respectively, for the SOC estimation. Additionally, the results for the SOH estimation show performance improvements of 65.95% and 64.36%, respectively, which are very accurate for BMS applications.

In conclusion, the proposed identification and co-estimation methods play a distinct and beneficial role in improving the accuracy of SOC and SOH co-estimation in lithium-ion batteries. Additionally, this study offers a theoretical framework for battery condition monitoring. In the real-world use of EVs, it offers significant contributions to real-time monitoring of their status to guarantee users' safety. However, the effects of aging on battery state estimation in actual driving conditions are not taken into account in this study. As a result, our future research will focus on considering the effects of battery aging on the SOC-SOH value of the lithium-ion battery, as well as improving the computational efficiency of the proposed model by eliminating some non-essential EEMDA method parameters.

CRediT authorship contribution statement

Paul Takyi-Aninakwa: Methodology, conceptualization, software, writing-original draft, analysis, and data curation; **Shunli Wang**: Supervision and resources; **Hongying Zhang**: Resources and investigation; **Xiao Yang**: Writing; **Carlos Fernandez**: Writing.

Declaration of competing interest

The authors declare that they have no known competing financial interests or personal relationships that could have appeared to influence the work reported in this paper.

Data availability

The authors do not have permission to share data.

Acknowledgments

The work is supported by the National Natural Science Foundation of China and the Natural Science Foundation of Southwest University of Science and Technology.

References

[1] Y. Wang, et al., A review of key issues for control and management in battery and ultra-capacitor hybrid energy storage systems, eTransportation (2020) 4.

[2] M. Kandidayeni, et al., Online power and efficiency estimation of a fuel cell system for adaptive energy management designs, Energy Convers. Manag. 255 (2022).

[3] P. Takyi-Aninakwa, et al., An optimized relevant long short-term memory-squared gain extended Kalman filter for the state of charge estimation of lithium-ion batteries, Energy 260 (2022) 1–15.

[4] K. Chayambuka, et al., Physics-based modeling of sodium-ion batteries part II. Model and validation, Electrochim. Acta (2022) 404.

[5] Y. Liu, et al., Interface equilibrium modeling of all-solid-state lithium-ion thin film batteries, J. Power Sources 454 (2020).

[6] T. Chen, et al., Applications of lithium-ion batteries in grid-scale energy storage systems, Trans. Tianjin Univ. 26 (3) (2020) 208–217.

[7] X. Sui, et al., A review of non-probabilistic machine learning-based state of health estimation techniques for Lithium-ion battery, Appl. Energy 300 (2021).

[8] E. Vanem, et al., Data-driven state of health modelling—A review of state of the art and reflections on applications for maritime battery systems, J.Energy Storage (2021) 43.

[9] M. Zhang, et al., Electrochemical impedance spectroscopy: a new chapter in the fast and accurate estimation of the state of health for lithium-ion batteries, Energies 16 (4) (2023).

[10] D. Andre, et al., Advanced mathematical methods of SOC and SOH estimation for lithium-ion batteries, J. Power Sources 224 (2013) 20–27.

[11] D.-I. Stroe, et al., Degradation behaviour of Lithium-ion batteries based on field measured frequency regulation mission profile, in: 2015 IEEE Energy Conversion Congress and Exposition (ECCE), 2015, pp. 14–21.

[12] C.B. Salucci, et al., A novel semi-supervised learning approach for state of health monitoring of maritime lithium-ion batteries, J. Power Sources 556 (2023) 1–11.

[13] Y. Guo, et al., Online estimation of SOH for lithium-ion battery based on SSA-Elman neural network, Protection and Control of Modern Power Systems 7 (1) (2022).

[14] A.V. Vykhodtsev, et al., A review of modelling approaches to characterize lithium-ion battery energy storage systems in techno-economic analyses of power systems, Renew. Sust. Energ. Rev. 166 (2022).

[15] X. Tang, et al., Joint estimation of state-of-charge and state-of-health for all cells in the battery pack using "leader-follower" strategy, eTransportation 15 (2023).

[16] P. Takyi-Aninakwa, et al., A hybrid probabilistic correction model for the state of charge estimation of lithium-ion batteries considering dynamic currents and temperatures, Energy 273 (2023).

[17] S. Zhang, et al., A rapid online calculation method for state of health of lithium-ion battery based on coulomb counting method and differential voltage analysis, J. Power Sources 479 (2020).

[18] H. Chaoui, S. Mandalapu, Comparative study of online open circuit voltage estimation techniques for state of charge estimation of lithium-ion batteries, Batteries 3 (4) (2017).

[19] J. Tian, et al., Battery state-of-charge estimation amid dynamic usage with physics-informed deep learning, Energy Storage Mater. 50 (2022) 718–729.

[20] P. Nian, Z. Shuzhi, Z. Xiongwen, Co-estimation for capacity and state of charge for lithium-ion batteries using improved adaptive extended Kalman filter, J. Energy Storage (2021) 40.

[21] W. Li, et al., Electrochemical model-based state estimation for lithium-ion batteries with adaptive unscented Kalman filter, J. Power Sources 476 (2020).

[22] Z. Ni, X. Xiu, Y. Yang, Towards efficient state of charge estimation of lithium-ion batteries using canonical correlation analysis, Energy 254 (2022).

[23] X. Fan, et al., SOC estimation of li-ion battery using convolutional neural network with U-net architecture, Energy 256 (2022).

[24] M. Esser, G. Rohde, C. Rehtanz, Electrochemical impedance spectroscopy setup based on standard measurement equipment, J. Power Sources 544 (2022).

[25] Y. Li, J. Chen, F. Lan, Enhanced online model identification and state of charge estimation for lithium-ion battery under noise corrupted measurements by bias compensation recursive least squares, J. Power Sources 456 (2020).

[26] P. Takyi-Aninakwa, et al., An optimized long short-term memory-weighted fading extended Kalman filtering model with wide temperature adaptation for the state of charge estimation of lithium-ion batteries, Appl. Energy 326 (2022).

[27] Z. Chen, et al., State of health estimation for lithium-ion batteries based on temperature prediction and gated recurrent unit neural network, J. Power Sources 521 (2022).

[28] J. Chen, et al., State of charge estimation of lithium-ion battery using denoising autoencoder and gated recurrent unit recurrent neural network, Energy 227 (2021).

[29] Y. Gong, et al., State-of-health estimation of lithium-ion batteries based on improved long short-term memory algorithm, J. Energy Storage (2022) 53.

[30] S. Wang, et al., An improved feedforward-long short-term memory modeling method for the whole-life-cycle state of charge prediction of lithium-ion batteries considering current-voltage-temperature variation, Energy 254 (2022).

[31] Q. Wang, et al., Deep convolutional neural network based closed-loop SOC estimation for lithium-ion batteries in hierarchical scenarios, Energy 261 (125718) (2022).

[32] J. Dou, et al., Extreme learning machine model for state-of-charge estimation of lithium-ion battery using salp swarm algorithm, J. Energy Storage (2022) 52.

[33] Q. Li, et al., State of health estimation of lithium-ion battery based on improved ant lion optimization and support vector regression, J. Energy Storage (2022) 50.

[34] C. Ge, Y. Zheng, Y. Yu, State of charge estimation of lithium-ion battery based on improved forgetting factor recursive least squares-extended Kalman filter joint algorithm, J. Energy Storage (2022) 55.

[35] M. Hossain, M.E. Haque, M.T. Arif, Kalman filtering techniques for the online model parameters and state of charge estimation of the Li-ion batteries: a comparative analysis, J. Energy Storage (2022) 51.

[36] P. Takyi-Aninakwa, et al., A strong tracking adaptive fading-extended Kalman filter for the state of charge estimation of lithium-ion batteries, Int. J. Energy Res. 46 (12) (2022) 16427–16444.

[37] W. He, et al., A physics-based electrochemical model for lithium-ion battery state-of-charge estimation solved by an optimised projection-based method and moving-window filtering, Energies 11 (8) (2018).

[38] J. Li, et al., A method for SOC estimation based on simplified mechanistic model for LiFePO4 battery, Energy 114 (2016) 1266–1276.

[39] B. Jiang, et al., Joint estimation of lithium-ion battery state of charge and capacity within an adaptive variable multi-timescale framework considering current measurement offset, Appl. Energy 253 (2019).

[40] K. Khodadadi Sadabadi, X. Jin, G. Rizzoni, Prediction of remaining useful life for a composite electrode lithium ion battery cell using an electrochemical model to estimate the state of health, J. Power Sources (2021) 481.

[41] X. Ding, et al., An improved thevenin model of lithium-ion battery with high accuracy for electric vehicles, Appl. Energy 254 (2019).

[42] Z. Ning, et al., Co-estimation of state of charge and state of health for 48 V battery system based on cubature Kalman filter and H-infinity, J. Energy Storage (2022) 56.

[43] L. Chen, et al., Adaptive state-of-charge estimation of lithium-ion batteries based on square-root unscented Kalman filter, Energy 252 (2022).

[44] L. Chen, et al., State of charge estimation of lithium-ion batteries based on fuzzy fractional-order unscented Kalman filter, Fractal Fraction. 5 (3) (2021).

[45] Z. Cui, et al., An extended Kalman filter based SOC estimation method for Li-ion battery, Energy Rep. 8 (2022) 81–87.

[46] C. Xu, et al., Dual fuzzy-based adaptive extended Kalman filter for state of charge estimation of liquid metal battery, Appl. Energy 327 (2022).

[47] K.A. Severson, et al., Data-driven prediction of battery cycle life before capacity degradation, Nat. Energy 4 (5) (2019) 383–391.

[48] X. Lai, et al., Co-estimation of state-of-charge and state-of-health for lithium-ion batteries considering temperature and ageing, Energies 15 (19) (2022).

[49] Y. Song, et al., A hybrid statistical data-driven method for on-line joint state estimation of lithium-ion batteries, Appl. Energy 261 (2020).

[50] B. Liu, X. Tang, F. Gao, Joint estimation of battery state-of-charge and state-of-health based on a simplified pseudo-two-dimensional model, Electrochim. Acta 344 (2020).

[51] J. Qiao, et al., A chaotic firefly - particle filtering method of dynamic migration modeling for the state-of-charge and state-of-health co-estimation of a lithium-ion battery performance, Energy 263 (2023).

[52] Y. Gao, et al., Enhanced state-of-charge estimation of LiFePO4 batteries using an augmented physics-based model, J. Power Sources 544 (2022).

[53] C. Wang, et al., A novel back propagation neural network-dual extended Kalman filter method for state-of-charge and state-of-health co-estimation of lithium-ion batteries based on limited memory least square algorithm, J. Energy Storage (2023) 59.

[54] W. Li, et al., Digital twin for battery systems: cloud battery management system with online state-of-charge and state-of-health estimation, J. Energy Storage (2020) 30.

[55] Y. Zou, et al., Combined state of charge and state of health estimation over lithium-ion battery cell cycle lifespan for electric vehicles, J. Power Sources 273 (2015) 793–803.

[56] R. Xiong, et al., Co-estimation of state of charge and capacity for lithium-ion batteries with multi-stage model fusion method, Engineering 7 (10) (2021) 1469–1482.

[57] Z. Wei, et al., A multi-timescale estimator for battery state of charge and capacity dual estimation based on an online identified model, Appl. Energy 204 (2017) 1264–1274.

[58] X. Tang, et al., A novel framework for Lithium-ion battery modeling considering uncertainties of temperature and aging, Energy Convers. Manag. 180 (2019) 162–170.

[59] H. Shi, et al., Improved multi-time scale lumped thermoelectric coupling modeling and parameter dispersion evaluation of lithium-ion batteries, Appl. Energy 324 (2022).

[60] D. Li, et al., Electrochemical impedance spectroscopy based on the state of health estimation for lithium-ion batteries, Energies 15 (18) (2022).

[61] F. Sun, R. Xiong, H. He, A systematic state-of-charge estimation framework for multi-cell battery pack in electric vehicles using bias correction technique, Appl. Energy 162 (2016) 1399–1409.

[62] B. Li, et al., A linear recursive state of power estimation method based on fusion model of voltage and state of charge limitations, J. Energy Storage (2021) 40.

[63] X. Lai, et al., Capacity estimation of lithium-ion cells by combining model-based and data-driven methods based on a sequential extended Kalman filter, Energy 216 (2021).

[64] H. Yang, et al., Remaining useful life prediction based on denoising technique and deep neural network for lithium-ion capacitors, eTransportation (2020) 5.

[65] G. Cheng, X. Wang, Y. He, Remaining useful life and state of health prediction for lithium batteries based on empirical mode decomposition and a long and short memory neural network, Energy 232 (2021).

[66] S. Son, et al., Integrated framework for SOH estimation of lithium-ion batteries using multiphysics features, Energy 238 (2022).

[67] W. Waag, S. Käbitz, D.U. Sauer, Experimental investigation of the lithium-ion battery impedance characteristic at various conditions and aging states and its influence on the application, Appl. Energy 102 (2013) 885–897.

[68] U. Tröltzsch, O. Kanoun, H.-R. Tränkler, Characterizing aging effects of lithium ion batteries by impedance spectroscopy, Electrochim. Acta 51 (8–9) (2006) 1664–1672.